Confining Sn nanoparticles in interconnected N-doped hollow carbon spheres as hierarchical zincophilic fibers for dendrite-free Zn metal anodes

Yu, Huan; Zeng, Yinxiang; Li, Nian Wu; Luan, Deyan; Yu, Le; Lou, David Xiong Wen

2022

https://hdl.handle.net/10356/160899

https://doi.org/10.1126/sciadv.abm5766

ELECTROCHEMISTRY

Confining Sn nanoparticles in interconnected N-doped hollow carbon spheres as hierarchical zincophilic fibers for dendrite-free Zn metal anodes

Huan Yu[1], Yinxiang Zeng[2], Nian Wu Li[1], Deyan Luan[2], Le Yu[1]*, Xiong Wen (David) Lou[2]*

We developed a three-dimensional hybrid fiber host consisting of interconnected N-doped hollow carbon spheres embedded with Sn nanoparticles (denoted as Sn@NHCF) for Zn metal anodes in high-performance Zn metal batteries. Experimental observations and density functional theory calculation reveal that the zincophilic Sn nanoparticles and N-doped carbons enable the homogeneous Zn deposition on the interior and exterior surfaces of the hollow fibers. Moreover, the hierarchical hollow fiber network effectively reduces the structural stress during the plating/stripping process. As a result, the developed Sn@NHCF host exhibits remarkable electrochemical properties in terms of high Coulombic efficiency, low voltage hysteresis, and prolonged cycling stability without dendrite formation. Moreover, a full cell based on the designed Sn@NHCF-Zn composite anode and a V_2O_5 cathode demonstrates superior rate capability and stable cycle life. This work provides a new strategy for the design of dendrite-free Zn anodes for practical applications.

INTRODUCTION

The ever-growing needs for renewable energy integration stimulate the enthusiasm of researchers to explore reliable, low-cost, and environmentally friendly electrochemical energy storage systems (EESs) (1). Among all available candidates, Zn-ion batteries (ZIBs) have been considered as the promising EES to replace the state-of-the-art dangerous/expensive Li-ion batteries (LIBs) and toxic lead-acid batteries (2–6). Metallic Zn is believed as the ideal anode for ZIBs owing to its superiorities such as chemical stability in water, abundant nature, low toxicity, high theoretical specific capacity (gravimetric and volumetric capacities of 820 mAh g^{-1} and 5855 mAh cm^{-3}, respectively), and low redox potential (−0.76 V versus standard hydrogen electrode) (7, 8). Nonetheless, the commercialization of high-performance Zn metal batteries still faces great obstructions, stemming from the uncontrolled formation of Zn dendrite and detrimental parasitic reactions. To be specific, the irregular local current density and hostless nature of the Zn deposition can induce the severe dendrite growth, thus resulting in poor cycling performance, low Coulombic efficiency (CE), and potential threat of short circuit (9–11). Besides, preferential dissolution of the dendrite root will lead to its detachment from the surface of Zn metal anode (ZMA), resulting in the irreversible consumption of active species. Moreover, undesirable side reactions such as hydrogen evolution reaction (HER) generate bubbles on ZMA, which influences the deposition morphology to form porous electrodeposits (12, 13). In addition, the noncompact nature of deposited Zn creates drastic volume change to increase the risk of cell failure (14).

The utilization of three-dimensional (3D) conductive skeletons has been considered as an effective strategy to restrain the dendrite growth via the regulation of local current distribution and Zn ion flux (15–19). Compared with planar configuration, the spatial confinement of 3D structure with enough space accommodates the volumetric changes to prolong the life span of ZMAs (20, 21). Nevertheless,

surface modulation is usually required to enable the 3D host with zincophilic nature and plenty of nucleation sites for reduced interfacial energy with Zn metal. Furthermore, component optimization is necessary to inhibit HER at the electrode/electrolyte interface. Among available candidates, carbonaceous materials stand out as ideal conductive substrates owing to their light weight and low cost for minimized additional mass (22–26). Graphitic carbons with low lattice mismatch for Zn might facilitate the epitaxial electrodeposition of Zn (27, 28). Some inspiring studies have been carried out to integrate carbon with other zincophilic species [pyridinic N (29), pyrrolic N (30), Ag (31, 32), etc.] to guide the uniform and reversible Zn deposition. However, the research of carbon-based 3D host for ZMAs is still at its fancy stage, and more explorations are necessary to further optimize their performance.

Here, we develop an effective hard-templating strategy for the design of a 3D fiber network structure consisting of adjacent N-doped hollow carbon spheres embedded with Sn nanoparticles (denoted as Sn@NHCF) as a composite host for ZMAs. Compared with bare Zn foil and conventional carbon substrates, the Sn@NHCF host exhibits apparent advantages. First, the 3D conductive framework with large surface area homogenizes the current distribution to promote relatively compact electrodeposition. Meanwhile, the hierarchical hollow fibers provide enough space for Zn deposition and enhance structural stability by buffering the volume expansion. The zincophilic Sn nanoparticles and N-doped carbons with low nucleation barriers and strong interactions with Zn^{2+} ensure the uniform deposition on the interior and exterior surfaces of the hollow fibers at low overpotential. Furthermore, Sn with weak electrocatalytic property toward HER prevents the generation of hydrogen bubbles within the cells. Benefiting from these superiorities, the Sn@NHCF electrode delivers low nucleation overpotential for dendrite-free Zn deposition with small voltage hysteresis and a prolonged cycling stability over 370 hours.

RESULTS

Formation process of Sn@NHCF

The synthesis procedure of Sn@NHCF is illustrated in Fig. 1A. Typically, homogeneous SiO_2 nanospheres with the average diameter

[1]State Key Laboratory of Organic-Inorganic Composites, Beijing University of Chemical Technology, Beijing 100029, P. R. China. [2]School of Chemical and Biomedical Engineering, Nanyang Technological University, 62 Nanyang Drive, Singapore 637459, Singapore.
*Corresponding author. Email: yule@mail.buct.edu.cn (L.Y.); xwlou@ntu.edu.sg (X.W.L.)
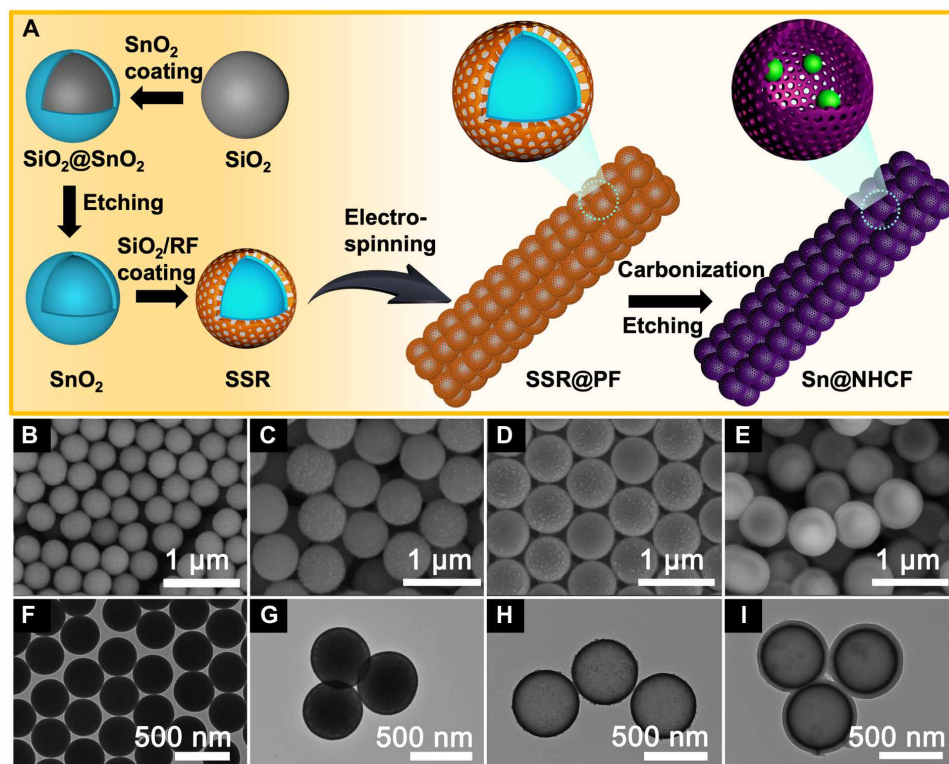
Fig. 1. Formation process of the Sn@NHCF host. (**A**) Schematic illustration of the synthesis of Sn@NHCF. (**B** to **E**) FESEM images and (**F** to **I**) TEM images of the SiO$_2$ nanospheres (B and F), SiO$_2$@SnO$_2$ core-shell nanospheres (C and G), SnO$_2$ hollow spheres (D and H), and SSR hollow spheres (E and I).

of about 430 nm are prepared as the hard template (Fig. 1, B and F). Next, a thin layer of SnO$_2$ is coated on SiO$_2$ nanospheres through the hydrolysis of Na$_2$SnO$_3$. The average diameter of the SiO$_2$@SnO$_2$ nanospheres increases to about 480 nm, suggesting that the thickness of SnO$_2$ sheath is around 25 nm (Fig. 1, C and G). After etching the SiO$_2$ cores, hollow SnO$_2$ nanospheres are obtained (Fig. 1, D and H). Then, a SiO$_2$/resorcinol-formaldehyde (RF) composite layer with a thickness of about 40 nm is coated on the SnO$_2$ hollow spheres, denoted as SSR hollow spheres (Fig. 1, E and I). The phase purity for each sample is confirmed by x-ray diffraction (XRD) investigations (fig. S1). During the electrospinning process, SSR hollow spheres self-assemble within polyacrylonitrile (PAN) to form the hierarchical fibers (denoted as SSR@PF). After the confined annealing of the SSR@PF and subsequent etching, interconnected N-doped carbon spheres embedded with numerous Sn nanoparticles are achieved as the 3D hollow fiber host, denoted as Sn@NHCF.

Characterization of Sn@NHCF

Field-emission scanning electron microscopy (FESEM) and transmission electron microscopy (TEM) observations reveal that the SSR hollow spheres can form a close-packed configuration with smooth surface along the long axis of PAN fibers during the electrospinning (Fig. 2, A to C). After the thermal treatment and the follow-up corrosion process, the Sn@NHCF sample retains the morphological features from the SSR@PFs without apparent external changes (Fig. 2D and fig. S2, A to C). However, the whole Sn@NHCF film experiences obvious shrinkage (fig. S3). The cross-sectional views indicate that the Sn@NHCF film has a thickness of about 130 μm with the average fiber

diameter of 1.2 μm (fig. S2, D and E). TEM images (Fig. 2E and fig. S2F) reveal prominent internal morphological evolution of Sn@NHCF after annealing. In particular, there are some irregular nanoparticles attached on internal shells. XRD patterns show the coexistence of carbon and metallic Sn phase [Joint Committee on Powder Diffraction Standards (JCPDS) no. 04-0673] within the Sn@NHCF sample, confirming the reduction of SnO$_2$ by the carbonaceous species (fig. S4). Meanwhile, the high-resolution TEM (HRTEM) images of Sn nanoparticles reveal the existence of (001) and (101) facets (fig. S5). Elemental mapping analysis in scanning TEM (STEM) mode indicates the spatial distribution of different elements within the hierarchical nanofibers. The high-angle annular dark field (HAADF)–STEM image (Fig. 2F) and the corresponding mapping results (Fig. 2, G to I) reveal the uniform distribution of C and N species throughout the hollow fibers. Meanwhile, Sn element shows a differentiated state. Apart from the fibers, Sn can also be observed on the agglomerating particles attached on the inner shells. On the basis of the above results, it can be deduced that these irregular particles with uneven sizes should be the reduced elemental Sn. As calculated from the thermogravimetric analysis (TGA), the weight ratio of Sn element in Sn@NHCF is about 45.7 weight % (fig. S6). X-ray photoelectron spectroscopy (XPS) measurement is used to analyze the chemical composition and valence state for Sn@NHCF (fig. S7). XPS survey spectrum proves the existence of Sn, C, and N elements in the Sn@NHCF composite. In particular, three fitting peaks can be clearly observed in the N 1s spectrum, which can be assigned to pyrrolic N (400.5 eV), pyridinic N (398.4 eV), and quaternary N (401.7 eV) (*26*). Raman spectrum provides the information about carbonaceous
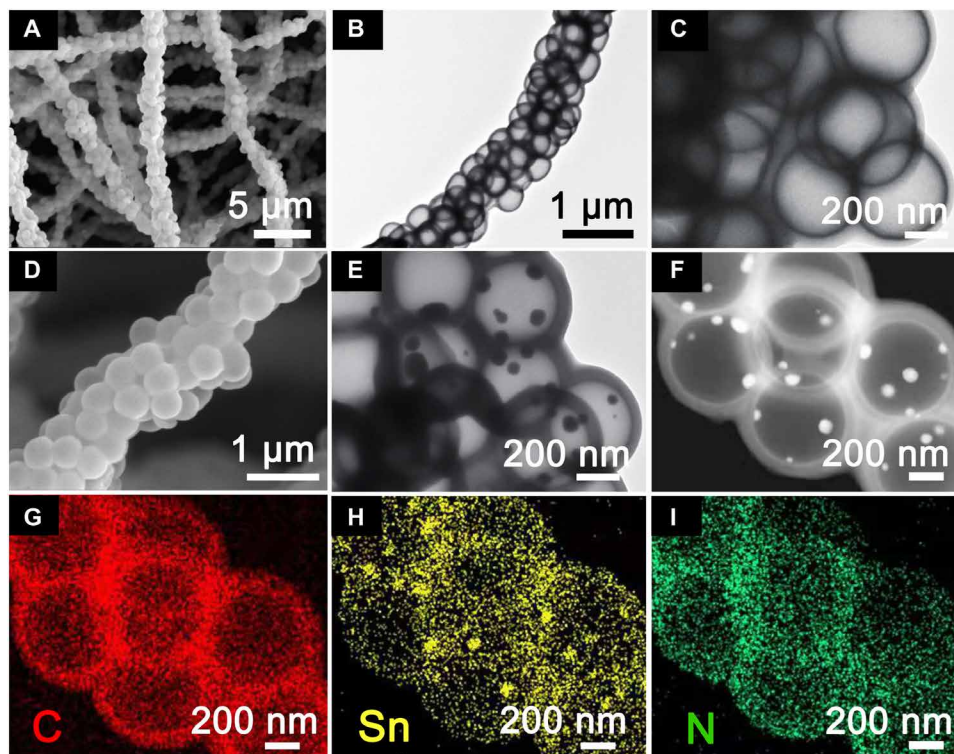
Fig. 2. Morphology characterization of SSR@PF and Sn@NHCF. (**A**) FESEM and (**B** and **C**) TEM images of SSR@PF. (**D**) FESEM and (**E**) TEM images of Sn@NHCF. (**F**) HAADF-STEM image and (**G** to **I**) the corresponding elemental mappings of an individual Sn@NHCF.

species within the Sn@NHCF (fig. S8). Both the D band and the G band can be detected with an I_D/I_G ratio of 2.24, suggesting the coexistence of the disordered or defect carbon and sp2 carbon. N_2 adsorption/desorption isotherms and pore size distribution reveal that the Sn@NHCF composite has a mesoporous structure with a Brunauer-Emmett-Teller surface area of 89.2 m^2 g^{-1} (fig. S9). The mesopores can allow the Zn^{2+} ions to move through the carbon shells and deposit into the hollow fibers.

Theoretical and electrochemical results of the Sn@NHCF host for ZMA

To understand the functional role of each component in Sn@NHCF for the nucleation and growth during the Zn deposition, we carry out density functional theory (DFT) calculations (Fig. 3A and fig. S10). The calculated binding energies (E_b) between Zn atoms and different species within the Sn@NHCF host are summarized in Fig. 3B. Impressively, Sn (101) exhibits the strongest E_b, indicating the zincophilic nature of the Sn nanoparticles. Besides, pyrrolic N also demonstrates better interaction with Zn than the carbon species as the zincophilic site. Furthermore, DFT-based interfacial charge-density results confirm the strongest affiliation between Sn and Zn with largest polarization at the interface (Fig. 3C). Owing to the strong affinity, aggregation of deposited Zn onto the surface of the Sn@NHCF host could be mitigated to avoid the generation of Zn dendrites. To verify these assumptions, we investigate the energy barriers of Zn nucleation on Sn@NHCF and Zn foil via Zn electroplating at a low current density of 1 mA cm^{-2} (Fig. 3D). For comparison, N-doped solid carbon fibers (NSCFs) without the addition of SSR hollow spheres, carbonized SSR on Ti foil (Sn/C-Ti), carbonized

SSR electrospun with polycaprolactone (PCL) (Sn/C@PCL), N-doped hollow carbon fibers (NHCFs), and commercial Sn foil are used to study the zincophilic feature for Sn species (fig. S11). Notably, the Sn@NHCF host exhibits a lower nucleation overpotential of only 11.4 mV than the Zn foil (64.2 mV) and NSCF (55.4 mV). In addition, the mass-transfer overpotential of Sn@NHCF (12.7 mV) is also much smaller than that of Zn foil (24.1 mV) and NSCF (26 mV), indicating better migration of Zn ions to the electrode surface (fig. S12) (*33*). The Sn@NHCF exhibits the lowest stripping overpotential among samples, further proving its superiorities as a Zn host (fig. S13). Cyclic voltammetry (CV) curves also prove that Sn@NHCF steadily induces the uniform Zn deposition with the smallest overpotential (fig. S14). Meanwhile, the control samples with Sn species (Sn foil, Sn/C-Ti, and Sn/C@PCL) exhibit lower nucleation overpotential than the NHCF (fig. S15). Moreover, the wettability tests of the $ZnSO_4$ electrolyte further demonstrate the enhanced Zn ion migration for the Sn@NHCF. As shown in Fig. 3E, the contact angle of electrolyte on the surface of Sn@NHCF is only 17.1°, much smaller than that of NSCF (48.8°) and Zn foil (63.3°; fig. S16). The notably decreased contact angle reflects the strong capillary actions on the Sn@NHCF surface, which is beneficial to the lateral growth of Zn crystals (*34*). Apart from the regulated Zn deposition, the Sn@NHCF also plays a critical role for the inhibition of the undesired HER. Linear sweep voltammetry (LSV) curves clearly show the low electrocatalytic activity of Sn@NHCF toward HER (Fig. 3F) (*35*). On the contrary, both NSCF and NHCF with N-doped carbon initiate the HER process profoundly (Fig. 3F and fig. S17A). Meanwhile, Zn foil can react with H_2SO_4 solution to generate H_2 bubbles (fig. S17B).
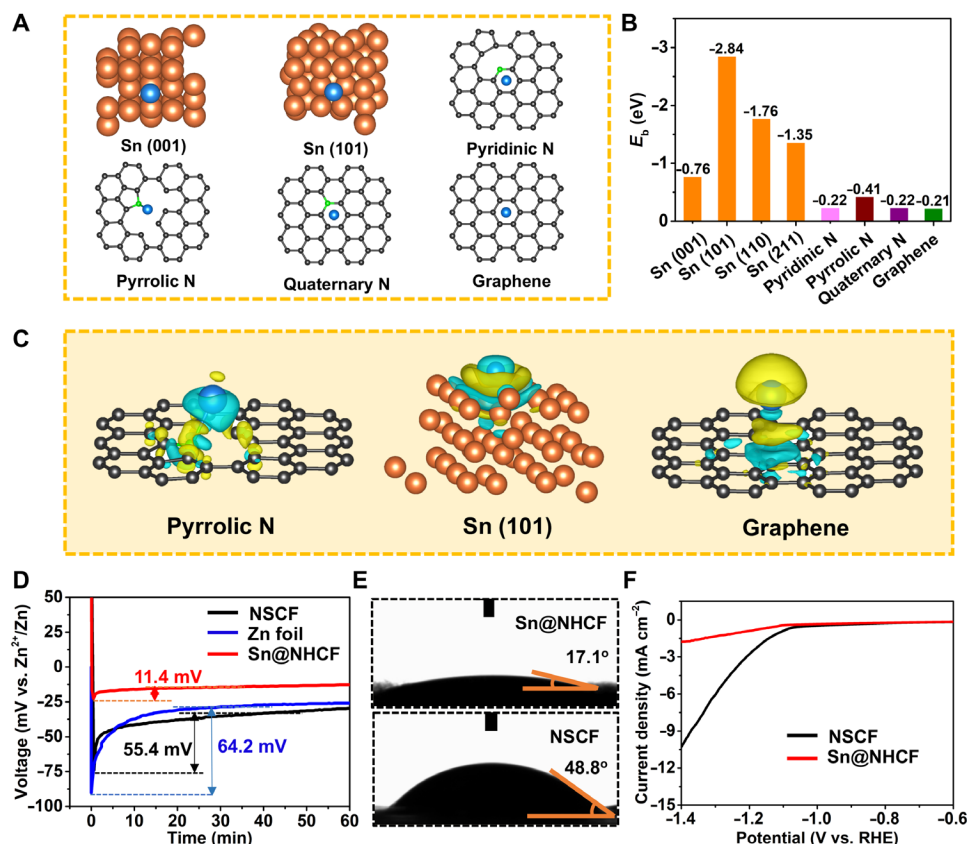
Fig. 3. Theoretical and electrochemical results of the Sn@NHCF host for ZMA. (**A**) Modeling of Sn, N-doped carbons, and graphene in DFT calculations. (**B**) Summary of the calculated E_b of Zn atom with Sn, N-doped carbons, and graphene. (**C**) Interfacial charge-density models of pyrrolic N, Sn (101), and graphene. (**D**) Voltage profiles of Zn plating on NSCF, Zn foil, and Sn@NHCF. (**E**) Wettability tests using ZnSO$_4$ electrolyte on Sn@NHCF and NSCF. (**F**) LSV curves of Sn@NHCF and NSCF for HER. All the potentials are referred to the reversible hydrogen electrode (RHE).

On the basis of the theoretical calculations and electrochemical results, Sn@NHCF displays great potential as the dendrite-free ZMA host (Fig. 4A). Owing to the high zincophilicity, small overpotential for nucleation/growth, and low HER activity, Sn@NHCF enables the uniform Zn deposition on both the exterior and interior surfaces without the generation of hydrogen bubbles. Besides, the hierarchical 3D hollow network provides sufficient space to store metallic Zn and effectively suppresses volume expansion during the repeated cycling. To validate the superiority of the Sn@NHCF host, we monitor the Zn deposition/stripping behaviors on different substrates in asymmetric cells. For the Zn foil, many vertical and sharp dendrites with a size of about 5 μm are formed after the Zn deposition and convert the planar surface into a sheet-like configuration (fig. S18). By sharp contrast, the Sn@NHCF host experiences negligible exterior changes after the Zn plating with a small capacity (Fig. 4, B and C). TEM analyses reveal that the contrast between the shell and the hollow interior becomes inconspicuous after the Zn deposition, indicating the preferential nucleation on the zincophilic Sn particles inside the hollow structures (fig. S19, A to C). On the contrary, the hollow spheres without agglomerated particles are still empty. Therefore, it can be deduced that the Sn in agglomerated form has a higher zincophilicity than the Sn species distributed throughout the fibers. According to the voltage profile of Zn plating on Sn@NHCF (fig. S19D) and Sn-Zn binary phase diagram (fig. S20), the deposited Zn particles tend to form a solid solution with Sn particles. XPS spectra

of Sn@NHCF-Zn disclose clear shifts of Sn 3d$_{5/2}$ and 3d$_{3/2}$ after the Zn deposition, testifying the strong interaction between Sn and deposited Zn (fig. S21) (36). After plating Zn at a higher capacity (5 mAh cm^{-2}), the deposited Zn can be found at both inner and exterior surfaces of Sn@NHCF (fig. S22, A and B). According to the enlarged TEM and HRTEM images and selected-area electron diffraction results (fig. S22, C to H), the deposited Zn particles are crystalline. The Zn (101) and Zn (100) facets are identified on the interior and exterior of the fibers, respectively. Meanwhile, large Sn nanoparticles still exist after the stripping processes (fig. S23). With the increase in Zn plating capacity, the porous network of the Sn@NHCF host is filled with deposited Zn without microsized dendrites (Fig. 4D). At the plating capacity of 12 mAh cm^{-2}, the average thickness of the Sn@NHCF-Zn is still around 130 μm, with the corresponding volumetric capacity of about 923.1 mAh cm^{-3} (fig. S24). Owing to the 3D conductive framework with reduced local current density and uniform electric field distribution, metallic Zn is guided and deposited within the host. Energy-dispersive x-ray spectroscopy (EDX) mapping and XRD pattern further prove the homogeneous Zn deposition inside the Sn@NHCF host (fig. S25). Because of the zincophilic nature, the deposited Zn particles serve as the nucleation sites for the subsequent Zn growth to form a layer-like structure within the void of Sn@NHCF fibers (fig. S26). Zn can be reversibly stripped from the Sn@NHCF host without any "dead Zn" and obvious structural damage (fig. S27). The inductively coupled plasma optical
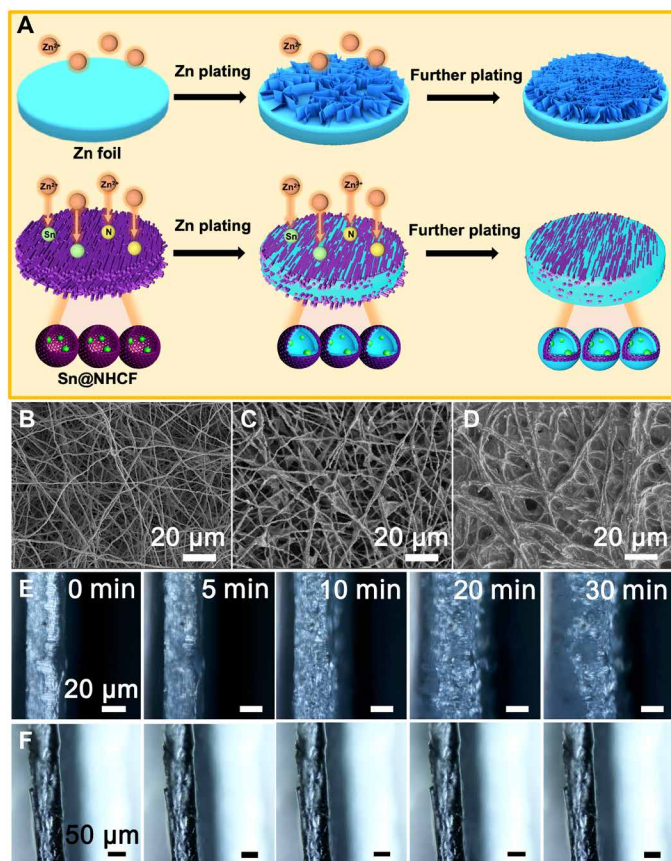
Fig. 4. Zn deposition behaviors on Sn@NHCF and Zn foil. (**A**) Schematic illustration of Zn deposition on the Zn foil and Sn@NHCF. FEESM images of the Sn@NHCF host (**B**) before and after Zn plating with a capacity of (**C**) 2 mAh cm^{-2} and (**D**) 12 mAh cm^{-2}. In situ optical observations of the Zn plating process on (**E**) Zn foil and (**F**) the Sn@NHCF host for different times at a current density of 10 mA cm^{-2}.
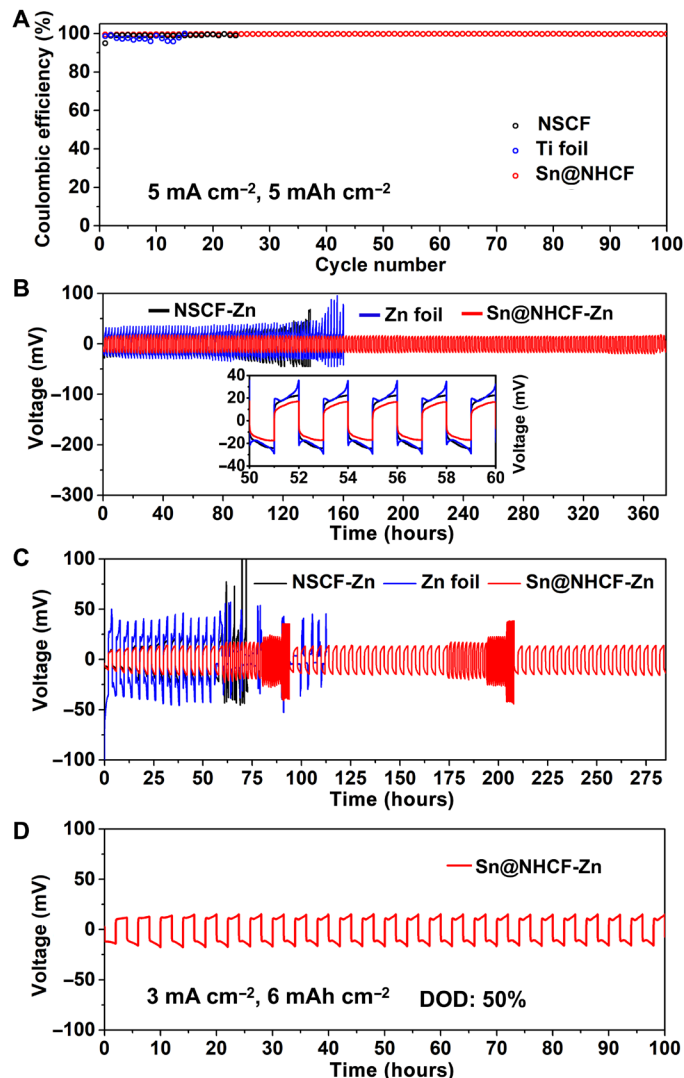

Fig. 5. Electrochemical performance of different electrodes. (**A**) CE plots of different hosts at a current density of 5 mA cm^{-2} with a capacity of 5 mAh cm^{-2}. (**B**) Galvanostatic discharge and charge voltage profiles of symmetric cells using different composite Zn electrodes and the enlarged voltage profiles (inset) at 1 mA cm^{-2} for 1 mAh cm^{-2}. (**C**) Galvanostatic discharge and charge voltage profiles of different cells at different current densities. (**D**) Galvanostatic discharge and charge voltage profiles of the symmetric cell using the Sn@NHCF-Zn electrode at 3 mA cm^{-2} for 6 mAh cm^{-2}.

emission spectroscopy (ICP-OES) results reveal that Sn nanoparticles are quite stable without formation of tin sulfate during the plating and stripping processes (table S1). On the contrary, large number of vertical and sharp sheet-like dendrites are formed on the surface of control samples after plating a high capacity of Zn (fig. S28). Before the deposition current density reaches to 8 mA cm^{-2}, there are no obvious dendrites on the Sn@NHCF host (fig. S29, A to C). At the current density of 1 mA cm^{-2}, the highest Zn capacity for Sn@NHCF host is 18 mAh cm^{-2} (fig. S29, D to F). In addition, in situ optical observations provide more direct evidence to support Sn@NHCF as a superior host (movie S1). To be specific, some small protrusions appear on the surface of Zn foil at the early stage of Zn plating (10 min) and rapidly evolve into Zn dendrites (Fig. 4E). Meanwhile, visible bubbles are produced on the surface of the NSCF host, confirming the possible hydrogen production (fig. S30 and movie S2). On the contrary, Sn@NHCF shows negligible changes with a smooth surface during the same plating process (Fig. 4F).

The plating and stripping performances of these electrodes are further evaluated using asymmetric cells. As shown in Fig. 5A, the Sn@NHCF host presents superior performances over NSCF and Zn foil with better cycling stability for 100 cycles and a high average CE of 99.7% at 5 mA cm^{-2} for 5 mAh cm^{-2}. The corresponding voltage hysteresis of the Sn@NHCF host is only 61.2 mV, much better than

that of bare Ti (102.2 mV) and NSCF (91.6 mV) (fig. S31). Furthermore, the CEs of Sn@NHCF host at 5 mA cm^{-2} maintain about 99.5% over 600 cycles and 99.8% over 200 cycles for capacities of 1 and 2 mAh cm^{-2}, respectively (fig. S32). Long-term cycling for the Sn@NHCF host is also investigated in symmetric cell after a pre-electrodeposition of Zn with a capacity of 12 mAh cm^{-2}. As a control, the same plating capacity is also applied for the NSCF host to form the NSCF-Zn electrode. At a current density of 1 mA cm^{-2}, the Sn@NHCF-Zn electrode owns a stable operation over 370 hours with a lower voltage hysteresis of 21 mV (Fig. 5B). However, the NSCF-Zn and Zn electrodes experience random voltage fluctuations and fast cell failures after cycling of about 116 and 147 hours, which might be attributed to the short circuit or detachment of

debris Zn. After 100 cycles of stripping/plating in symmetric cells, obvious dendrites are generated on the cycled NSCF-Zn (fig. S33A) and Zn foil (fig. S33B). By contrast, the cycled Sn@NHCF-Zn electrode keeps a smooth surface without dendrite even after 300 cycles (fig. S33, C to F). Besides, the Sn@NHCF-Zn electrode shows good rate performances with steadily increased voltage hysteresis at different current densities from of 0.5 to 5 mA cm^{-2}, which is superior to NSCF-Zn and Zn foil (Fig. 5C and fig. S34). Even at higher areal capacities and higher depth-of-discharge (DOD) values, the symmetric cells using Sn@NHCF-Zn electrodes still exhibit stable operation (fig. S35, A and B). It is worth noting that the symmetric cell can achieve stable cycling over 100 hours at a higher areal capacity of 6 mAh cm^{-2} (DOD, 50%) at 3 mA cm^{-2} (Fig. 5D). Moreover, Sn@NHCF-Zn electrodes also demonstrate stable cycling when the capacity of the pre-electroplated Zn is reduced to 8 mAh cm^{-2} (fig. S35C) and 4 mAh cm^{-2} (fig. S35D). The electrochemical performance of Sn@NHCF-Zn is comparable to that of many previous studies using different hosts (table S2) (15, 23–25, 27, 37–39).

To explore the feasibility of the Sn@NHCF host in practical applications, we use commercial V_2O_5 (fig. S36) as the cathode to assemble a full battery (Fig. 6A). Rate performance of the Sn@NHCF-Zn||V_2O_5 and Zn||V_2O_5 cells is presented in Fig. 6B. At a low current density of 0.2 A g^{-1}, the Sn@NHCF-Zn||V_2O_5 and Zn||V_2O_5 cells exhibit similar average discharge capacities of 236.4 and 224.5 mAh g^{-1}, respectively. With the increase in current density, the Sn@NHCF-Zn||V_2O_5 cell still delivers superior discharge capacities of 171.6, 142.7, 127.3, and 95.3 mAh g^{-1} at the current densities of 0.5, 1, 3, and 5 A g^{-1}, respectively (Fig. 6C). As a comparison, the discharge capacity of the Zn||V_2O_5 cell quickly decreases to only 60.8 mAh g^{-1} at 5 A g^{-1}. Although there are similar redox peaks for both cells, a narrower voltage gap for the Sn@NHCF-Zn||V_2O_5 cell can be found, revealing the smaller polarization (Fig. 6D). In addition, electrochemical impedance spectroscopy (EIS) spectra also show that the Sn@NHCF-Zn||V_2O_5 cell exhibits lower charge-transfer resistance for the promoted ion diffusion kinetics (fig. S37). Moreover, the cycling performances of cells at a V_2O_5 mass loading of 1.2 mg cm^{-2} are examined at 1 A g^{-1}
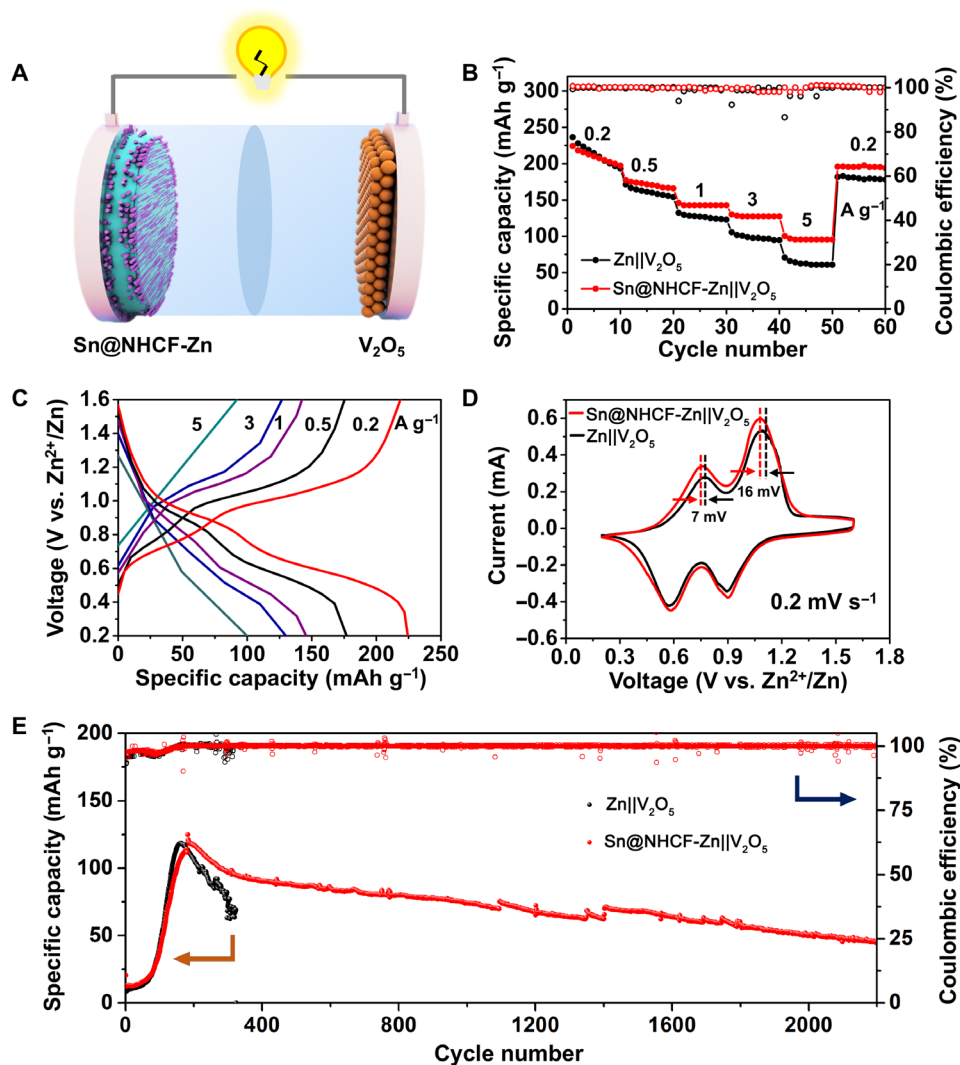

Fig. 6. Electrochemical performance of different electrodes in full cells. (**A**) Schematic illustration of the Sn@NHCF-Zn||V_2O_5 cell. (**B**) Rate performances of the Sn@NHCF-Zn||V_2O_5 and Zn||V_2O_5. (**C**) Discharge and charge voltage profiles of the Sn@NHCF-Zn||V_2O_5 at different rates. (**D**) CV curves of the Sn@NHCF-Zn||V_2O_5 and Zn||V_2O_5 with a V_2O_5 mass loading of 1.2 mg cm^{-2}. (**E**) Cycling performances of the Sn@NHCF-Zn||V_2O_5 and the Zn||V_2O_5 with a V_2O_5 mass loading of 5 mg cm^{-2} at a current density of 1 A g^{-1}.

(fig. S38). After the similar capacity increase in the initial cycles related to the activation of the Zn^{2+} intercalation process (*35, 40, 41*), the Sn@NHCF-Zn||V_2O_5 cell provides a higher capacity retention over 1200 cycles with a high CE of almost 100%. On the basis of the mass of cathode, the gravimetric energy densities of Zn||V_2O_5 and Sn@NHCF-Zn||V_2O_5 are 163.6 and 206.6 mWh g^{-1}, respectively. When the mass loading of V_2O_5 is increased to 5 mg cm^{-2}, the Sn@NHCF-Zn||V_2O_5 cell still manifests stable operation over 2000 cycles with high CE. By contrast, the Zn||V_2O_5 cell experiences fast capacity decay within 350 cycles (Fig. 6E). These results further confirm the superiority of the Sn@NHCF-Zn as the composite Zn anode.

DISCUSSION

In summary, we reported a 3D hollow fiber network as a dendrite-free Zn host via an effective multistep strategy. The interconnected N-doped carbon hollow spheres embedded with Sn nanoparticles serve as the zincophilic framework with weak electrocatalytic activity toward water splitting. Owing to the reduced local current density, strong interaction with Zn, and promoted ion transfer, the Sn@NHCF host regulates the nucleation and growth behavior for the uniform Zn deposition on the exterior and interior surfaces of the fiber with small overpotential. The plenty void spaces within the hollow fibers relieve the structural stress for a long-term cycling over 370 hours. This work might shed some light on the design of high-performance Zn anodes in practical applications.

MATERIALS AND METHODS
Synthesis of SiO$_2$ nanospheres
All the chemicals were purchased and used without further purification. In a typical synthesis, 50 ml of ethanol and 24 ml of ammonia (Sinopharm Chemical Reagent Co. Ltd.) were mixed under stirring. Then, 4.2 ml of tetraethyl orthosilicate (TEOS; Sinopharm Chemical Reagent Co. Ltd.) was added to this solution and stirred at 40°C for 1 hour. The product was collected by centrifugation at 5000 rpm for 5 min, washed with ethanol several times, and dried at 60°C for 24 hours. The amount of SiO_2 was around 1.1 g.

Synthesis of SiO$_2$/SnO$_2$ nanospheres
The synthetic route followed the previously reported work with slight modifications (*42*). First, 1.8 g of urea (Aladdin) and 0.266 g of $Na_2SnO_3 \cdot 3H_2O$ (Aladdin) were dissolved in 34 ml of deionized (DI) water under stirring for 30 min. Then, 18 ml of ethanol was added and stirred for another 2 hours as suspension A. Meanwhile, 0.3 g of SiO_2 spheres was dispersed in 4 ml of DI water by ultrasonication as suspension B. These two suspensions were mixed, transferred to a Teflon-lined stainless steel autoclave, and then heated to 170°C for 36 hours. After cooling down, the product was centrifuged, washed with DI water, and dried at 60°C for 24 hours. The amount of SiO_2/ SnO_2 nanospheres was around 0.42 g.

Synthesis of SnO$_2$ hollow nanospheres
The SiO_2 cores were etched in 2 M NaOH (Sinopharm Chemical Reagent Co. Ltd.) at 45°C under continuous magnetic stirring (stirring speed, 100 rpm) for 16 hours. After cooling down, the product was centrifuged and dried at 60°C. The amount of SnO_2 hollow nanospheres was around 0.13 g.

Synthesis of SSR
The synthetic route followed the previously reported work with slight modifications (*43*). SnO_2 hollow spheres (0.25 g) were dispersed in 35 ml of DI water. Then, 15 ml of ethanol was added. Next, the resorcinol (0.16 g, Aladdin), formaldehyde (0.24 ml, Aladdin), and ethylenediamine (EDA) (0.16 ml, Aladdin) were successively added. After stirring for 5 min, 0.1 ml of TEOS was added. The above system was further mixed under stirring at 30°C for 24 hours. Afterward, the product was harvested via centrifugation, washed by DI water and ethanol several times, and dried at 60°C. The amount of SSR was around 0.2 g.

Synthesis of SSR@PF
SSR (1.3 g) was dispersed in 3 ml of dimethylformamide (DMF; Aladdin) via sonication for 1 hour and stirring for 4 hours as solution A. PAN [0.8 g; molecular weight (MW) ~150,000; Sigma-Aldrich] was dispersed in 4 ml of DMF and then heated to 60°C under continuous magnetic stirring for 5 hours as solution B. Then, solution A and solution B were mixed under stirring at 60°C overnight. The above solution was loaded into a syringe using a stainless steel nozzle, which was connected to a high-voltage power supply. The high voltage, feeding rate, temperature, and distance between the anode and the cathode were fixed at 18 kV, 1.0 ml $hour^{-1}$, 40°C, and 18 cm, respectively. Afterward, the obtained film was dried at 200°C for 1 hour. Then, the film was cut into round disks with a diameter of 1.2 cm, and the mass of single disk was around 3.8 mg.

Synthesis of Sn@NHCF
SSR@PF was annealed at 700°C for 4 hours under the protection of N_2 atmosphere and then etched in 2 M NaOH at 45°C for 2 hours to remove SiO_2 species. The ramping rate was set at 1°C min^{-1}. Lastly, the Sn@NHCF product was washed by DI water and ethanol several times and dried in air at 60°C for further use.

Synthesis of NSCF
PAN (0.8 g) was dispersed in 7 ml of DMF under continuous magnetic stirring at 60°C for 5 hours. The above solution was loaded into a syringe using a stainless steel nozzle, which was connected to a high-voltage power supply. The high voltage, feeding rate, temperature, and distance between the anode and the cathode were fixed at 18 kV, 1.0 ml $hour^{-1}$, 40°C, and 18 cm, respectively. Afterward, the film was dried at 200°C for 1 hour and then annealed at 700°C for 4 hours under the protection of N_2 atmosphere to obtain the NSCF product. The ramping rate was set at 1°C min^{-1}.

Synthesis of Sn/C hollow spheres
One gram of SSR spheres was annealed at 700°C for 4 hours under the protection of N_2 to obtain Sn/C hollow spheres. Note that this Sn/C sample contains some SiO_x from the decomposition of TEOS.

Synthesis of Sn/C@PCL
One gram of Sn/C was added into the mixed solution of 3 ml of dichloromethane (Sigma-Aldrich) and 7 ml of DMF under continuous stirring to form homogeneous solution. Then, 7.3 mg of cetyl trimethyl ammonium bromide (Sigma-Aldrich) and 3 g of PCL (MW = 80,000 to 90,000; Sigma-Aldrich) were added into the above solution and mixed homogeneously. The above solution was loaded into a syringe using a stainless steel nozzle, which was connected to a high-voltage power supply. The high voltage, feeding rate, temperature, and distance

between the anode and the cathode were fixed at 20 kV, 1.0 ml hour^{-1}, 40°C, and 18 cm, respectively.

Synthesis of NHCF

SiO$_2$ spheres (0.25 g) were dispersed in 35 ml of DI water. Then, 15 ml of ethanol was added. Next, 0.16 g of resorcinol, 0.24 ml of formaldehyde, and 0.16 ml of EDA were successively added. After stirring for 5 min, 0.1 ml of TEOS was added. The above system was further mixed under stirring at 30°C for 24 hours. Afterward, the product was harvested via centrifugation, washed by DI water and ethanol several times, and dried at 60°C. Obtained precursor (1.3 g) was dispersed in 3 ml of DMF via sonication for 1 hour and stirring for 4 hours as solution A. PAN (0.8 g) was dispersed in 4 ml of DMF and then heated to 60°C under continuous magnetic stirring for 5 hours as solution B. Then, solution A and solution B were mixed under stirring at 60°C overnight. The above solution was loaded into a syringe using a stainless steel nozzle, which was connected to a high-voltage power supply. The high voltage, feeding rate, temperature, and distance between the anode and the cathode were fixed at 18 kV, 1.0 ml hour^{-1}, 40°C, and 18 cm, respectively. Afterward, the film was dried at 200°C for 1 hour, then annealed at 700°C for 4 hours under the protection of N$_2$ atmosphere, and then etched in 2 M NaOH at 45°C for 12 hours to remove SiO$_2$.

Material characterizations

The morphology of the samples was investigated with FESEM (TESCAN Clara; JEOL JSM7800F) and TEM (JEOL, HT7700) equipped with EDX. The crystal structure was tested by XRD on a Bruker D2 Phaser x-ray diffractometer with Ni-filtered Cu Kα radiation (λ = 1.5406 Å) at a voltage of 30 kV and a current of 10 mA. The surface chemical states of the samples were examined by an ESCALAB 250 XPS system with an Al Kα radiation source. Raman spectrum was collected through a Renishaw inVia Raman microscope equipped with a Leica DMIRBE inverted optical microscope using the laser excitation source at 514 nm. TGA was carried out under air with a ramping rate of 5°C min^{-1}. The N$_2$ sorption measurement was carried on Autosorb 6B at −196°C. The content of elements was measured by an ICP-OES (Thermo Fisher Scientific, iCAP 7000).

Electrochemical characterizations

The deposition and stripping behaviors of Zn were conducted in a two-electrode electrochemical cell on a CHI660E electrochemical workstation using the Sn@NHCF host as the working electrode and Zn foil as the counter/reference electrode. CR2032-type coin cells were assembled to evaluate CE using the Sn@NHCF host, Ti foil, and NSCF as the working electrodes; Zn foil as the counter electrode; and glass fiber as the separator. The areal mass of the Sn@NHCF architecture was about 1.86 mg cm^{-2}. The average thickness and mass of Zn foil were 200 μm and 161.2 mg, respectively. Meanwhile, the average thickness and mass of NSCF were 90 μm and 1.8 mg, respectively. For symmetric cells, metallic Zn (12 mAh cm^{-2}) was pre-electroplated into the Sn@NHCF hosts at 2 mA cm^{-2} as Sn@NHCF-Zn electrodes with a total mass of about 17.84 mg. Before CE tests in the asymmetric cells and cycling tests in symmetric cells, one activation cycle was taken at the small current density of 0.1 mA cm^{-2} for 1 mAh cm^{-2} to stabilize these samples. The commercial Sn foil was bought from Anhui Zesheng Technology Co. Ltd. For the Sn/C-Ti electrode, Sn/C hollow spheres, Super P carbon black, and poly-vinylidene fluoride (PVDF) were mixed with a weight ratio of 7:2:1

into N-methyl-2-pyrrolidone (NMP) solvent. The homogeneous slurry was cast onto the Ti foil and dried in the vacuum oven overnight at 80°C. The mass loading of active Sn/C species was about 2 mg cm^{-2}. As for the full cell tests, the Sn@NHCF-Zn or Zn foil anode was re-assembled against a V$_2$O$_5$ cathode. For the preparation of cathode slurry, V$_2$O$_5$ powder (Sigma-Aldrich), Super P carbon black, and PVDF were mixed with a weight ratio of 7:2:1 into NMP solvent. The homogeneous slurry was cast onto the Ti foil and dried in the vacuum oven overnight at 80°C. The mass loading of active V$_2$O$_5$ species was about 1.2 or 5.0 mg cm^{-2}. All electrodes were cut into round disks with a diameter of 1.2 cm. For the above electrochemical experiments, 2.0 M ZnSO$_4$ aqueous solution was used as electrolyte. EIS measurements were conducted in the range of 0.01 to 10^6 Hz with an amplitude of 0.01 V. For HER, 0.1 M H$_2$SO$_4$ solution was used as electrolyte. Meanwhile, a carbon rod and a Ag/AgCl electrode were used as the counter electrode and the reference electrode, respectively.

In situ optical observations

In situ observations were carried out in an optical cell with quartz window (E001, Tianjin Aida Hensheng Technology Development Co., Ltd). After assembly in ZnSO$_4$ solution using Zn foil and the Sn@NHCF host, the cell was sealed with a fluorine rubber ring. An optical microscopy (BX53MRF-S Japan) with a fitted charge-coupled device camera was applied to monitor the Zn deposition process.

Calculation methods

First-principles calculations were performed on the basis of the DFT coupled with the Vienna Ab initio Simulation Package. The generalized gradient approximation in the formulation of Perdew-Burke-Ernzerhof was used to treat the exchange and correlation energy. The cutoff energy of 450 eV was adopted for the wave basis sets. The grid spacings of k points used in the Brillouin zone for geometry optimization and density of states were 0.04 and 0.08 Å^{-1}, respectively. The force and energy were converged to 0.02 eV Å^{-1} and 2.0×10^{-5} eV, respectively. The cutoff energy of 450 eV was set for the plane-wave basis. Moreover, a 3 × 3 supercell was built in this work, and a Γ-centered k-point sampling grid of 2 × 2 × 1 was adopted here. The vacuum layer with a thickness of 20 Å was applied to avoid virtual interaction. The adsorption energy was calculated according to the following equation

$$E_{ads} = E_{total} - E_{surf} - E_{Zn} \tag{1}$$

where E_{total} and E_{surf} are the total energy of the system and the surface, respectively, and E_{Zn} is the energy of the Zn atom.

SUPPLEMENTARY MATERIALS

Supplementary material for this article is available at https://science.org/doi/10.1126/sciadv.abm5766

REFERENCES AND NOTES

1. N. Kittner, F. Lill, D. M. Kammen, Energy storage deployment and innovation for the clean energy transition. *Nat. Energy* **2**, 17125 (2017).
2. L. Ma, M. A. Schroeder, O. Borodin, T. P. Pollard, M. S. Ding, C. Wang, K. Xu, Realizing high zinc reversibility in rechargeable batteries. *Nat. Energy* **5**, 743–749 (2020).
3. B. Dunn, H. Kamath, J. M. Tarascon, Electrical energy storage for the grid: A battery of choices. *Science* **334**, 928–935 (2011).
4. J. T. Huang, J. Zhou, S. Q. Liang, Guest pre-intercalation strategy to boost the electrochemical performance of aqueous zinc-ion battery cathodes. *Acta Phys. Chim. Sin.* **37**, 2005020 (2021).

5. J. Guan, N. W. Li, L. Yu, Artificial interphase layers for lithium metal anode. *Acta Phys. Chim. Sin.* **37**, 2009011 (2021).

6. Q. N. Zhu, Z. Y. Wang, J. W. Wang, X. Y. Liu, D. Yang, L. W. Cheng, M. Y. Tang, Y. Qin, H. Wang, Challenges and strategies for ultrafast aqueous zinc-ion batteries. *Rare Met.* **40**, 309–328 (2021).

7. J. X. Zheng, L. A. Archer, Controlling electrochemical growth of metallic zinc electrodes: Toward affordable rechargeable energy storage systems. *Sci. Adv.* **7**, eabe0219 (2021).

8. C. P. Li, X. S. Xie, S. Q. Liang, J. Zhou, Issues and future perspective on zinc metal anode for rechargeable aqueous zinc-ion batteries. *Energy Environ. Mater.* **3**, 146–159 (2020).

9. V. Yufit, F. Tariq, D. S. Eastwood, M. Biton, B. Wu, P. D. Lee, N. P. Brandon, Operando visualization and multi-scale tomography studies of dendrite formation and dissolution in zinc batteries. *Joule* **3**, 485–502 (2019).

10. Q. Yang, G. Liang, Y. Guo, Z. Liu, B. Yan, D. Wang, Z. Huang, X. Li, J. Fan, C. Zhi, Do zinc dendrites exist in neutral zinc batteries: A developed electrohealing strategy to in situ rescue in-service batteries. *Adv. Mater.* **31**, 1903778 (2019).

11. S. Higashi, S. W. Lee, J. S. Lee, K. Takechi, Y. Cui, Avoiding short circuits from zinc metal dendrites in anode by backside-plating configuration. *Nat. Commun.* **7**, 11801 (2016).

12. F. Wang, O. Borodin, T. Gao, X. Fan, W. Sun, F. Han, A. Faraone, J. A. Dura, K. Xu, C. Wang, Highly reversible zinc metal anode for aqueous batteries. *Nat. Mater.* **17**, 543–549 (2018).

13. V. Verma, S. Kumar, W. Manalastas, M. Srinivasan, Undesired reactions in aqueous rechargeable zinc ion batteries. *ACS Energy Lett.* **6**, 1773–1785 (2021).

14. B. Y. Tang, L. T. Shan, S. Q. Liang, J. Zhou, Issues and opportunities facing aqueous zinc-ion batteries. *Energy Environ. Sci.* **12**, 3288–3304 (2019).

15. Q. Zhang, J. Luan, X. Huang, L. Zhu, Y. Tang, X. Ji, H. Wang, Simultaneously regulating the ion distribution and electric field to achieve dendrite-free Zn anode. *Small* **16**, 2000929 (2020).

16. Y. Yin, S. Wang, Q. Zhang, Y. Song, N. Chang, Y. Pan, H. Zhang, X. Li, Dendrite-free zinc deposition induced by tin-modified multifunctional 3D host for stable zinc-based flow battery. *Adv. Mater.* **32**, 1906803 (2020).

17. J. F. Parker, C. N. Chervin, I. R. Pala, M. Machler, M. F. Burz, J. W. Long, D. R. Rolison, Rechargeable nickel-3D zinc batteries: An energy-dense, safer alternative to lithium-ion. *Science* **356**, 415–418 (2017).

18. P. Zhao, B. Yang, J. Chen, J. Lang, T. Zhang, X. Yan, A safe, high-performance, and long-cycle life zinc-ion hybrid capacitor based on three-dimensional porous activated carbon. *Acta Phys. Chim. Sin.* **36**, 1904050 (2020).

19. Q. Zhang, J. Luan, L. Fu, S. Wu, Y. Tang, X. Ji, H. Wang, The three-dimensional dendrite-free zinc anode on a copper mesh with a zinc-oriented polyacrylamide electrolyte additive. *Angew. Chem. Int. Ed.* **58**, 15841–15847 (2019).

20. Y. An, Y. Tian, S. Xiong, J. Feng, Y. Qian, Scalable and controllable synthesis of interface-engineered nanoporous host for dendrite-free and high rate zinc metal batteries. *ACS Nano* **15**, 11828–11842 (2021).

21. Z. Shen, L. Luo, C. Li, J. Pu, J. Xie, L. Wang, Z. Huai, Z. Dai, Y. Yao, G. Hong, Stratified zinc-binding strategy toward prolonged cycling and flexibility of aqueous fibrous zinc metal batteries. *Adv. Energy Mater.* **11**, 2100214 (2021).

22. Y. Tian, Y. An, C. Liu, S. Xiong, J. Feng, Y. Qian, Reversible zinc-based anodes enabled by zincophilic antimony engineered MXene for stable and dendrite-free aqueous zinc batteries. *Energy Storage Mater.* **41**, 343–353 (2021).

23. Y. Zeng, X. Zhang, R. Qin, X. Liu, P. Fang, D. Zheng, Y. Tong, X. Lu, Dendrite-free zinc deposition induced by multifunctional CNT frameworks for stable flexible Zn-ion batteries. *Adv. Mater.* **31**, 1903675 (2019).

24. Z. Wang, J. Huang, Z. Guo, X. Dong, Y. Liu, Y. Wang, Y. Xia, A metal-organic framework host for highly reversible dendrite-free zinc metal anodes. *Joule* **3**, 1289–1300 (2019).

25. Y. Tian, Y. An, C. Wei, B. Xi, S. Xiong, J. Feng, Y. Qian, Flexible and free-standing Ti$_3$C$_2$T$_x$ MXene@Zn paper for dendrite-free aqueous zinc metal batteries and nonaqueous lithium metal batteries. *ACS Nano* **13**, 11676–11685 (2019).

26. T. Lin, I.-W. Chen, F. Liu, C. Yang, H. Bi, F. Xu, F. Huang, Nitrogen-doped mesoporous carbon of extraordinary capacitance for electrochemical energy storage. *Science* **350**, 1508–1513 (2015).

27. Q. H. Cao, H. Gao, Y. Gao, J. Yang, C. Li, J. Pu, J. Du, J. Yang, D. Cai, Z. Pan, C. Guan, W. Huang, Regulating dendrite-free zinc deposition by 3D zincopilic nitrogen-doped vertical graphene for high-performance flexible Zn-ion batteries. *Adv. Funct. Mater.* **31**, 2103922 (2021).

28. J. Zheng, Q. Zhao, T. Tang, J. Yin, C. D. Quilty, G. D. Renderos, X. Liu, Y. Deng, L. Wang, D. C. Bock, C. Jaye, D. Zhang, E. S. Takeuchi, K. J. Takeuchi, A. C. Marschilok, L. A. Archer, Reversible epitaxial electrodeposition of metals in battery anodes. *Science* **366**, 645–648 (2019).

29. F. X. Xie, H. Li, X. Wang, X. Zhi, D. Chao, K. Davey, S.-Z. Qiao, Mechanism for zincophilic sites on zinc-metal anode hosts in aqueous batteries. *Adv. Energy Mater.* **11**, 2003419 (2021).

30. C. Li, Z. Sun, T. Yang, L. Yu, N. Wei, Z. Tian, J. Cai, J. Lv, Y. Shao, M. H. Rümmeli, J. Sun, Z. Liu, Directly grown vertical graphene carpets as Janus separators toward stabilized Zn metal anodes. *Adv. Mater.* **32**, 202003425 (2020).

31. Y. Zhang, J. D. Howe, S. Ben-Yoseph, Y. Wu, N. Liu, Unveiling the origin of alloy-seeded and nondendritic growth of Zn for rechargeable aqueous Zn batteries. *ACS Energy Lett.* **6**, 404–412 (2021).

32. T. Chen, Y. Wang, Y. Yang, F. Huang, M. Zhu, B. T. W. Ang, J. M. Xue, Heterometallic seed-mediated zinc deposition on inkjet printed silver nanoparticles toward foldable and heat-resistant zinc batteries. *Adv. Funct. Mater.* **31**, 2101607 (2021).

33. L. Luo, J. Li, H. Y. Ast, A. Manthiram, A 3D lithiophilic Mo$_2$N-modified carbon nanofiber architecture for dendrite-free lithium-metal anodes in a full cell. *Adv. Mater.* **31**, 1904537 (2019).

34. S. Li, J. Fu, G. Miao, S. Wang, W. Zhao, Z. Wu, Y. Zhang, X. Yang, Toward planar and dendrite-free Zn electrodepositions by regulating Sn-crystal textured surface. *Adv. Mater.* **33**, 2008424 (2021).

35. L. Wang, W. Huang, W. Guo, Z. H. Guo, C. Chang, L. Gao, X. Pu, Sn alloying to inhibit hydrogen evolution of Zn metal anode in rechargeable aqueous batteries. *Adv. Funct. Mater.* **32**, 2108533 (2022).

36. Z. Hou, Y. Gao, H. Tan, B. A. Zhang, Realizing high-power and high-capacity zinc/sodium metal anodes through interfacial chemistry regulation. *Nat. Commun.* **12**, 3083 (2021).

37. G. Zhang, X. Zhang, H. Liu, J. Li, Y. Chen, H. Duan, 3D-printed multi-channel metal lattices enabling localized electric-field redistribution for dendrite-free aqueous Zn ion batteries. *Adv. Energy Mater.* **11**, 2003927 (2021).

38. P. Xue, C. Guo, N. Wang, K. Zhu, S. Jing, S. Kong, X. Zhang, L. Li, H. Li, Y. Feng, W. Gong, Q. Li, Synergistic manipulation of Zn^{2+} ion flux and nucleation induction effect enabled by 3D hollow SiO$_2$/TiO$_2$/Carbon fiber for long-lifespan and dendrite-free Zn-metal composite anodes. *Adv. Funct. Mater.* **21**, 2007388 (2021).

39. N. N. Zhang, S. Huang, Z. Yuan, J. Zhu, Z. Zhao, Z. Niu, Direct self-assembly of MXene on Zn anodes for dendrite-free aqueous zinc-ion batteries. *Angew. Chem. Int. Ed.* **60**, 2861–2865 (2021).

40. P. Liang, J. Yi, X. Liu, K. Wu, Z. Wang, J. Cui, Y. Liu, Y. Wang, Y. Xia, J. Zhang, Highly reversible Zn anode enabled by controllable formation of nucleation sites for Zn-based batteries. *Adv. Funct. Mater.* **30**, 1908528 (2020).

41. W. Guo, Z. Cong, Z. Guo, C. Chang, X. Liang, Y. Liu, W. Hu, X. Pu, Dendrite-free Zn anode with dual channel 3D porous frameworks for rechargeable Zn batteries. *Energy Storage Mater.* **30**, 104–112 (2020).

42. X. W. Lou, C. L. Yuan, L. A. Archer, Shell-by-shell synthesis of tin oxide hollow colloids with nanoarchitectured walls: Cavity size tuning and functionalization. *Small* **3**, 261–265 (2007).

43. Z. Li, J. T. Zhang, B. Y. Guan, X. W. Lou, Mesoporous carbon@titanium nitride hollow spheres as an efficient SeS$_2$ host for advanced Li-SeS$_2$ batteries. *Angew. Chem. Int. Ed.* **56**, 16003–16007 (2017).

Science Advances

Confining Sn nanoparticles in interconnected N-doped hollow carbon spheres as hierarchical zincophilic fibers for dendrite-free Zn metal anodes

Huan YuYinxiang ZengNian Wu LiDeyan LuanLe YuXiong Wen (David) Lou

View the article online
https://www.science.org/doi/10.1126/sciadv.abm5766
Permissions
https://www.science.org/help/reprints-and-permissions

Use of this article is subject to the Terms of service